EUROFUSION WPDIV-PR(15) 14614

J.H. You et al.

Loading nature and failure features of a conventional water-cooled divertor target

Preprint of Paper to be submitted for publication in
Nuclear Fusion

This work has been carried out within the framework of the EUROfusion Consortium and has received funding from the Euratom research and training programme 2014-2018 under grant agreement No 633053. The views and opinions expressed herein do not necessarily reflect those of the European Commission.

Loading nature and failure features of a conventional water-cooled divertor target

Jeong-Ha You*, Muyuan Li

1. Introduction

The plasma-facing components (PFCs) are subjected to variable high heat flux (HHF) loads which can amount up to 10-20 MW/m². Moreover, material embrittlement due to neutron irradiation is one of the most critical issues. The neutron irradiation dose of the DEMO divertor is predicted to be higher than that of the ITER by an order of magnitude [1, 2]. Moreover, the pulse duration time of plasma burning in a DEMO reactor will be significantly longer than in the ITER. Such a long pulse operation may foster damage such as creep-fatigue or irradiation creep at high temperatures [3-5]. Since the structural performance of the PFC materials will be dictated by temperature-dependent mechanical properties, the impact of thermal boundary condition (HHF loads and cooling condition) on the structural behavior needs to be assessed to identify the maximum possible power exhaustion capability. In this context, quantitative assessment and the understanding of major failure modes is of importance. In this review article, this topic is discussed on the basis of computational studies.

2. Performance of the divertor PFC materials

The ITER-type divertor target is the baseline design concept being currently considered for the European DEMO divertor targets with the options of advanced design variants. The plasma-facing unit of the ITER-type divertor target consists of W armor monoblocks joined with a CuCrZr cooling tube as heat sink where both parts are bonded via a Cu interlayer. The typical geometry of the ITER-type target (the left symmetric half of a monoblock unit) is illustrated in Fig. 1 where the dimension of the W block is 23×22×4 mm^3. The inner diameter of the tube is 12 mm. The thickness of the W armor, CuCrZr tube and Cu interlayer are 5, 1 and 0.5 mm, respectively.

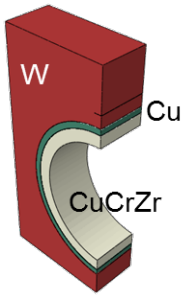

Fig. 1. Schematic of the water-cooled target model (symmetric half) considered for FEA. W armor block: 23 mm×22 mm×4 mm, cooling tube thickness: 1 mm, inner diameter: 12 mm, Cu interlayer thickness: 0.5 mm.

To deal with the materials issues related to the divertor target design, it is necessary to understand the thermal and mechanical performance of the baseline materials (CuCrZr alloy, W) under neutron irradiation. Although the amount of available test data is quite limited, basic features and trends can be found as summarized in the following.

2.1. CuCrZr alloy [6-9]

- Substantial thermal recovery of irradiation damage, if the temperature of irradiation (1-10 dpa) is higher than ca. 250 °C. Above 300 °C ductility is fully recovered.
- Strong hardening and embrittlement when irradiated below 150 °C. The uniform elongation is negligible.
- In the transition temperature range between 150 and 250 °C, considerable capability of total elongation (ca. 6 %) before rupture. But, the load bearing capability decreases with strain.
- Significant loss of strength at elevated temperatures above ca. 350 °C owing to over-ageing and irradiation creep after long-term thermal exposure.
- Sufficient fracture toughness even after irradiation. Toughness decreases with temperature exhibiting only slight dose-dependence.

2.2. Tungsten [10]

- Ductile-to-brittle transition (DBT) behavior occurring between ca. 600 and 900 °C. The DBT temperature is

sensitively dependent on strain rate, microstructure and irradiation dose.

- Marginal capability of plastic deformation below the DBTT even without irradiation.
- Recrystallization at ca. 1300 °C leading to significant embrittlement and softening.

2.3. Implication on structural design

The features of the mechanical performance of CuCrZr and W described above suggest that both materials will have to be used for an allowed operation temperature range, respectively, to avoid brittle fracture or plastic failure. Generally, this requirement is strictly respected in design practice, particularly for structural materials. In the present case, the heat sink tube is the structural part. Thus, the desired temperature window for CuCrZr alloy should be considered as mandatory. In terms of ductility and strength, the optimal temperature range lies between 250 °C and 300 °C.

However, the paramount requirement of power exhaust is to avoid any coolant burnout accident even under slow transient events, which sets the upper bound onto the coolant temperature. In the case of current water-cooled divertor design for DEMO, this upper limit is roughly 150 °C. Moreover, the corrosion-erosion issue requires that the coolant temperature should be kept as low as possible, say, below 150 °C [11]. Therefore, the structural design of the heat sink tube needs to accept a non-ductile operation regime below 250 °C possibly down to 150 °C.

Regarding the tungsten armor, there is no established design rule yet in the currently available design codes. As the water-cooled tungsten armor is to be operated with a wide temperature range from far below the DBT temperature to far above recrystallization temperature, one cannot apply a desired temperature window to the monoblock type armor.

3. Thermal response of an ITER-type water-cooled divertor target

To derive materials requirements for divertor PFCs, the thermal loading nature needs to be characterized at first. In this chapter, the thermal response of a typical ITER-like divertor target is briefly discussed.

A typical temperature field building up in the cooling tube during typical HHF loading is illustrated in Fig. 2. Plotted is the temperature field under the HHF load at 18 MW/m² standing for a slow transient event (coolant temperature: 150 °C). It is seen that the HHF loading produces a steep temperature gradient along the tube periphery as well as through the thickness at the upper position.

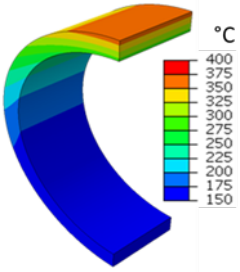

Fig. 2. Temperature field produced in the cooling tube during steady state HHF loading (heat flux load: 18 MW/m², coolant temperature of 150 °C) [12].

In Table 1, the computed temperature values are listed calculated for three different heat flux loads (10, 15 and 18 MW/m²) and a fixed coolant temperature (150 °C) [12]. The presented data indicate the temperatures at four selected positions in the tube: the uppermost bond interface, the uppermost inner wall, the side bond interface, and the side inner wall.

Table 1. Computed cooling tube temperatures at four selected positions (coolant temperature: 150 °C) [12].

Heat flux load (MW/m²)	10	15	18
interface at the top (°C)	263	316	348
inner wall at the top	229	266	288
interface at the side	172	181	187
inner wall at the side	169	177	182

From these data following trends can be found:

1. The maximum temperature at the uppermost bond interface of the CuCrZr tube seems acceptable up to 15 MW/m² and marginal from 15 to 18 MW/m². Higher heat flux loads would cause severe irradiation creep of the CuCrZr tube leading to premature rupture.
2. The temperature at the uppermost inner wall ranging from 229 °C to 288 °C seems to be high enough to be a potential concern in terms of corrosion issue. However, the corrosion risk could be mitigated by lower coolant temperature.
3. The temperatures at the side region of the tube seem acceptable, if the total elongation criterion or a non-ductile fracture mechanics criterion can be applied for the structural design.
4. For the assumed coolant temperature (150 °C), the optimal heat flux load for the CuCrZr tube is thought to lie around 10 MW/m², provided that the corrosion issue is not critical. For the heat flux loads higher than 15 MW/m², advanced Cu alloys or Cu composites will have to be employed.

4. Structural loading behavior of an ITER-type water-cooled divertor target

4.1. Cyclic stress and deformation in the cooling tube

Fig. 3 shows the axial (a) and the hoop component (b) of the thermal stress produced in the cooling tube after 10 HHF cycles at 18 MW/m² (coolant: 150 °C) [12].

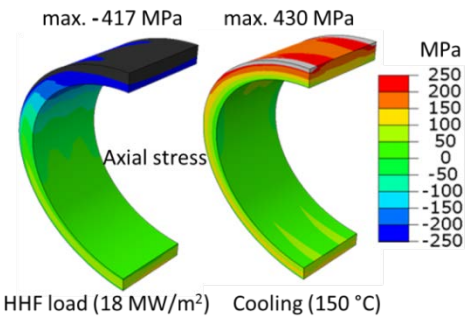

(a)

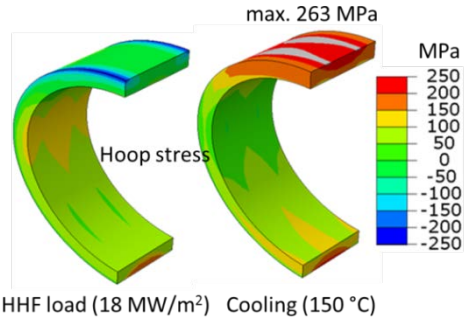

(b)

Fig. 3. Axial component (a) and hoop component (b) of the thermal stress field produced in the cooling tube after 10 HHF load cycles (heat flux load: 18 MW/m², coolant temperature of 150 °C) [12].

It is noted that thermal stresses (including the residual stress) are produced by the differential thermal strain mismatch between the W armor block and the CuCrZr cooling tube. Since the thermal stresses outweigh the static membrane stress due to the coolant pressure, we consider only the secondary stresses for our discussion about the structural reliability of the divertor heat sink. It is found that critical tensile stresses build up during the cooling phase whereas compressive longitudinal stress prevails during HHF heating. The stresses are concentrated mainly in the upper region of the tube whereas in the rest part of the tube the stresses remain rather moderate or weak during both the HHF loading as well as cooling. The stress concentration appearing at the edge of the bond interface may possibly initiate fatigue failure or interfacial debonding. At the upper interface edge the stress state varies periodically from compressive to tensile upon the shut-off of the cyclic HHF loads (and vice versa upon the onset of the HHF loads). This means that the interface edge region will experience reversed loading that may possibly cause fatigue damage during pulsed HHF operation. In the bulk region away from the edge the stress intensity is relatively lower than in the edge region, but still high enough to trigger non-ductile failures of the CuCrZr tube being embrittled under neutron irradiation.

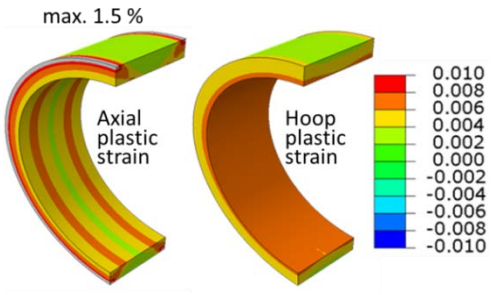

Fig. 4. Axial (left) and hoop (right) component of the plastic strain field produced in the tube after 10 HHF load cycles (heat flux load: 18 MW/m², coolant temperature of 150 °C) [12].

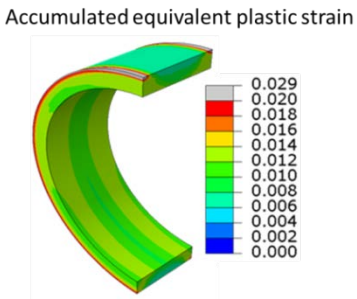

Fig. 5. Accumulated equivalent plastic strain produced in the tube after 10 HHF load cycles (heat flux load: 18 MW/m², coolant temperature of 150 °C) [12].

Figs. 4 and 5 show the plastic strain fields produced in the cooling tube after ten HHF loading cycles at 18 MW/m² (coolant temperature: 150 °C) [12]. Plotted are the axial (left) and the hoop (right) component (Fig. 4) and the accumulated equivalent plastic strain (Fig. 5). The figures reveal that plastic strain is concentrated locally in the edge region of the bond interface. It is noted that the plastic strain state is not altered from the residual strain state during subsequent HHF loading. It means that no further plastic yield takes place during the subsequent HHF heating under which the stress sign is periodically reversed.

A rigorous cyclic plasticity simulation shows that the plastic straining of the cooling tube occurs only during the fabrication process, provided that the CuCrZr alloy used for the tube does not undergo overaging (ripening of the precipitates) or irradiation creep (dissolution of the precipitates) during subsequent thermal exposure under the HHF loads and neutron irradiation so that the initial prime-aged microstructure and thus the initial yield strength are preserved. In this case, considerable residual stress can be produced due to the differential thermal strain mismatch during cooling in the joining process. Concomitantly, overall plastic yield occurs in the tube. The intensity of the residual stress depends on the thermal history, in particular, the effective stress free temperature of the fabrication process.

The presence of strong residual stress can significantly influence the further evolution of thermal stress during the HHF loading, as the secondary stress produced by the HHF loads is superposed onto the residual stress. Assuming a precipitation-hardened state of the CuCrZr tube, the high yield stress of the CuCrZr alloy leads to an accordingly high residual stress (ca. 300-400 MPa), which dominates over the secondary stress of opposite sign.

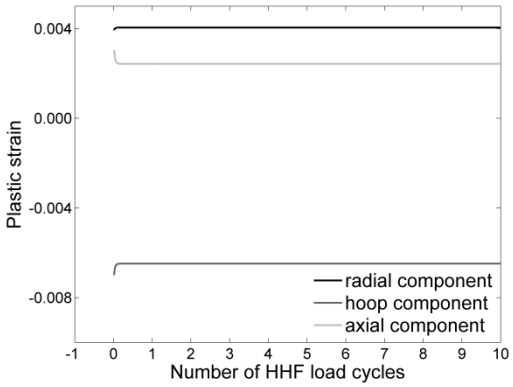

Fig. 6. History of the principal plastic strains in the cooling tube during 10 HHF load cycles (heat flux load: 18 MW/m², coolant temperature of 150 °C) [12].

This feature is well demonstrated in Fig. 6 where the temporal variation of three principal plastic strains (expressed in a cylindrical coordinate system adapted to the tube geometry) is plotted over the first 10 HHF load cycles at 18 MW/m² (coolant temperature: 150 °C). It is seen that the stress state in the cooling tube readily enters into the fully elastic shakedown regime already upon the onset of the 'first' HHF load so that no further plastic deformation takes place anymore during the subsequent cyclic HHF loading following the first load cycle. In this circumstance, the risk of

plastic fatigue or ratchetting can be excluded. It is reminded that this condition can be met, only if the CuCrZr tube does not undergo softening due to overaging or irradiation creep at a maximum operation temperature. The upper temperature limit to avoid such effect lies between 300 – 350 °C. The corresponding heat flux load would range from 14 to 18 MW/m². Should a part of the tube be subjected to still higher temperatures beyond this limit in long-term operation, the CuCrZr tube would possibly undergo a significant plastic fatigue due to softening by irradiation creep and overaging.

4.2. Low cycle fatigue of Cu interlayer

In contrast to the CuCrZr cooling tube, the soft copper interlayer was shown to undergo heavy plastic fatigue (i.e. low cycle fatigue) due to large variation of plastic deformation already in the early stage of HHF loading.

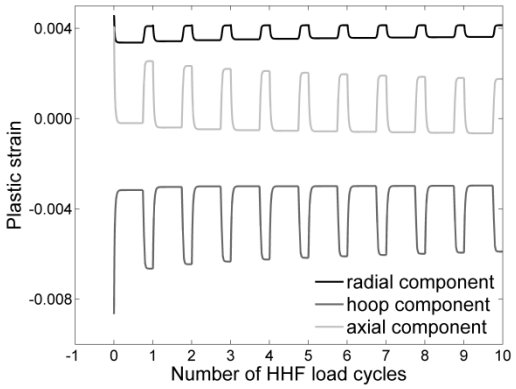

Fig. 7. History of the principal plastic strains in the Cu interlayer during 10 HHF load cycles (heat flux load: 18 MW/m², coolant temperature of 150 °C) [12].

This feature is illustrated in Fig. 7 where the periodic temporal variation of three principal plastic strains (in a cylindrical coordinate system) is plotted. It is found that the radial and axial components exhibit quite large plastic strain amplitudes whereas the hoop component has a roughly constant magnitude. The fatigue lifetime (the number of cycles to failure due to plastic fatigue) can be estimated using the plastic strain amplitudes on the basis of Manson-Coffin type fatigue life data. For the present ITER-type target model, the estimates are as follows (coolant temperature: 150 °C):

3600 cycles at 10 MW/m²

1200 cycles at 15 MW/m²

720 cycles at 18 MW/m²

This result indicates that the plastic fatigue of the Cu interlayer may pose a critical design concern in terms of the structural reliability of the whole target PFC, if the design specification for the envisaged number of HHF pulses requires larger numbers than the predicted fatigue life for the stationary and slow transient phases, respectively.

4.3. Deep cracking of W armor block

Several recent HHF test campaigns performed on ITER divertor target mock-ups demonstrated that W armor blocks were vulnerable to macroscopic cracking, when the applied cyclic HHF loads were raised to 20 MW/m² which corresponds to the peak heat flux during slow transient events (loss of plasma detachment) [13]. HHF fatigue loads at 20 MW/m² often produced a deep crack through individual W blocks. The cracks were normally initiated on the top surface being heated and grew further downward even often reaching the cooling tube. The mechanism of the deep cracking phenomena was clarified by the authors in a computational study based on fracture mechanics, where the crack initiation was attributed to plastic fatigue while the subsequent crack growth was shown to be a result of tensile stress concentration at the crack tip [14]. The strong tensile stress field at the crack tip appears during the cooling stage until the crack grows up to ca. 4.5 mm long depth downwards. On the other hand, if the crack becomes larger than 5.5 mm, then the tensile stress field at the crack tip develops during the HHF heating stage. This fracture feature is visually illustrated in Fig. 8 where the thermal stress fields (horizontal component) in the cross section of the target PFC are plotted for the HHF loading (20 MW/m²) and the cooling (150 °C) phase, respectively. The stress fields are presented for three different sizes of crack (1.5, 3.5 and 5.5 mm). It is seen

that the upper region of the armor is compressed during the HHF loading (crack is closed) while tensile stress states prevail in this region during the cooling (crack is opened). Fig. 8 reveals that the stress state and the intensity of the singular stress field at the crack tip varies with the crack depth.

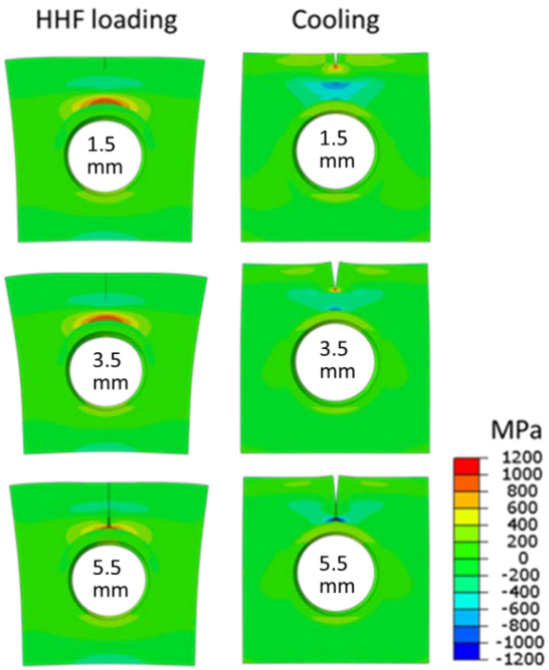

Fig. 8. Thermal stress fields (horizontal component) in the cross section of the target PFC plotted for the HHF loading (20 MW/m²) and the cooling (150 °C) phase, respectively. (Crack size: 1.5, 3.5 and 5.5 mm)

Fig. 9 and 10 show the J-integral values at the crack tip computed as a function of crack lengths ranging from 0.5 mm to 5.5 mm from the top surface [14]. J-integral is a direct measure of crack tip loading indicating the driving force for crack extension. In Fig. 9 and 10 the J-integral values at two positions of the crack front (free surface end and symmetry center) are presented for the HHF loading (20 MW/m²) and the cooling (150 °C) case, respectively. A common feature is that the crack tip loading is stronger at the mid of the crack front (i.e. armor interior) than at the free surface edge.

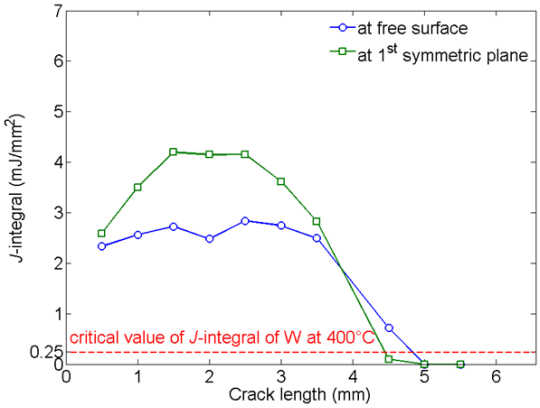

Fig. 9. J-integral values of a vertical crack in the W armor during cooling (150 °C) computed as a function of crack lengths [14].

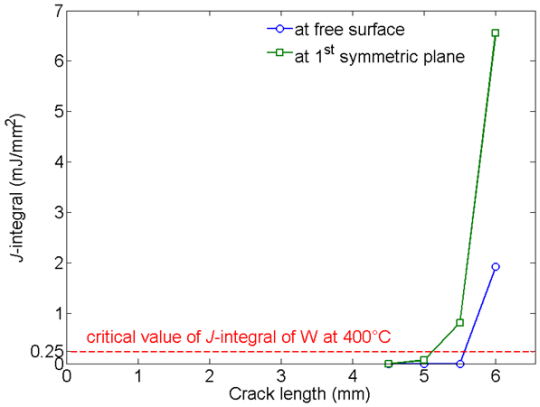

Fig. 10. J-integral values of a vertical crack in the W armor during HHF heating (20 MW/m²) computed as a function of crack lengths [14].

Fig. 9 shows that the crack tip J-integral values during the cooling stage are sufficiently high compared to the critical fracture energy (or toughness) of the tungsten armor (ca. 0.25 kJ/m²) in the depth range up to ca. 4.5 mm so that the crack can grow further up to 4.5 mm in the repeated cooling phases, once it has been initiated at the surface.

On the other hand, Fig. 10 shows that during the HHF heating phase the J-integral begins to increase rapidly only after the crack size has reached 5.5 mm reaching the critical values. This means that HHF loading at 20 MW/m² can produce critical crack tip loads exceeding the toughness, but only for a deep crack larger than 5.5 mm. In the depth range between 4.5 mm to 5.5 mm, the J-integral decreases below the critical fracture energy in both the cooling and HHF heating phases. Thus, the

most probable crack length is expected to lie within this depth range.

It is noted that the surface crack is initiated by plastic fatigue. In an extreme HHF loading case (20 MW/m²) as assumed above, significant fatigue may take place in the surface layer since this region is subjected to large plastic strain amplitudes and tensile stress in the initial transient stage of cooling. The fatigue life estimated for the HHF load of 20 MW/m² is less than 90 load cycles. Such a significant fatigue effect is attributed to the low yield stress of tungsten in the surface layer caused by recrystallization. It was observed that the recrystallized depth amounted ca. 4 mm under 20 MW/m² [13].

If there is no recrystallization-induced plastic fatigue on the armor surface, the highest tensile stress intensity in the W armor appears near the bond interface to the CuCrZr tube. Under neutron irradiation tungsten will experience not only embrittlement but also reduction of strength. Once W armor undergoes such degradation, the tensile stress in the armor near the bond interface can exceed the reduced fracture strength of irradiated W leading to crack initiation. This alternative cracking scenario is demonstrated in Fig. 11 where the cracking patterns were simulated by means of XFEM (extended finite element method) technique [15]. Here, the color code scales with the damage parameter.

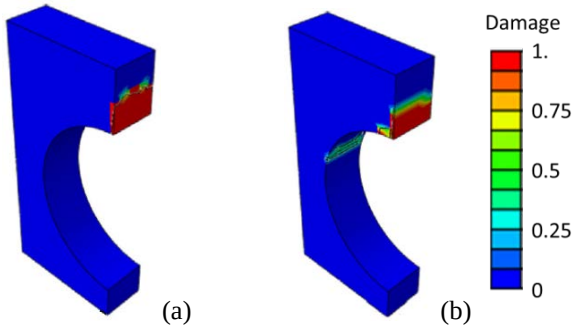

Fig. 11. Brittle cracking patterns of W armor block after HHF loading at 15 MW/m² (a) and 18 MW/m² (b), respectively. Coolant temeparture is 150 °C, and the assumed tensile fracture stress is 600 MPa. Damage parameter value of unity (red color) indicates complete seperation of the crack faces [15].

The damage parameter of unity and the red-color code denote complete seperation of the crack faces. Here, the fracture strength was assumed to be 600 MPa. This value corresponds to 40 % decrease compared to the unirradiated case. The figures manifest that cracks can be initiated and grow in radial direction from the bond interface to the tube as well, when the tensile fracture strength and toughness of W is significantly decreased by irradiation.

Fig. 12 plots the computed stress intensity factor values of a radial crack in the W armor block initiated at the interface to the tube as a function of angular position along the hoop direction around the tube (null degree denotes the uppermost position) [15]. The three curves denote the K factor values for three crack lengths (0.5, 1, 1.5 mm), respectively. The assumed HHF load was 15 MW/m² with a coolant temperature of 150 °C. For comparison, the toughness value of a typical tungsten material (10 MPa √m) is also indicated as a dotted line.

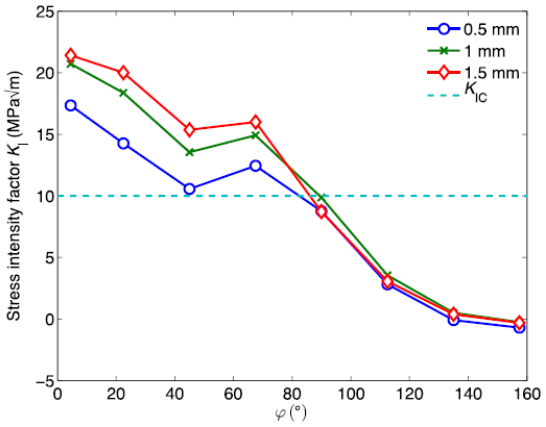

Fig. 12. Computed stress intensity factor values of a radial crack in the W armor block initiated at the interface to the tube as a function of angular position along the circumferential direction around the tube (null degree denotes the uppermost position). HHF load: 15 MW/m², coolant temperature: 200 °C.

The peak stress intensity factor of a radial crack in the W armor near the uppermost tube position is twice the toughness of (unirradiated) W. It means that the driving force for crack growth surpasses the toughness, once a radial crack has been formed near the upper part of the tube reaching a critical length of several hundred µm.

4.4. Surface cracking of W armor under thermal shock

W armor will also be exposed to characteristic thermal shock loads during transient instabilities such as ELMs (Edge Localized Modes). The thermal loads by ELMs are predicted to be frequent (~1 Hz), short (~1 ms) and extremely intense (GW/m²) releasing huge amount of thermal power (~1 MJ) onto the surface. In many HHF fatigue tests simulating the ELM-like thermal shocks, characteristic surface cracking features were observed [16, 17]. They showed that a network of many short cracks was created on the W armor surface where the typical crack depth ranged from several tens of μm to a few hundreds of μm (see the micrograph in Fig. 13).

In computational fracture mechanics studies, the crack patterns observed experimentally could be reproduced by use of XFEM simulation [18, 19]. Fig. 13 presents an example illustrating a predicted crack path produced by HHF shock load of 1.27 GW/m² with pulse duration of 1 ms. For the XFEM simulation, a cylindrical model was used as armor (thickness: 5 mm). The radius of the heat-loaded surface area was assumed to be 2.26 mm. The peak temperature at the loaded surface (i.e. central area) was 2550 °C. In the figure a cross section with thermal residual stress field is also plotted.

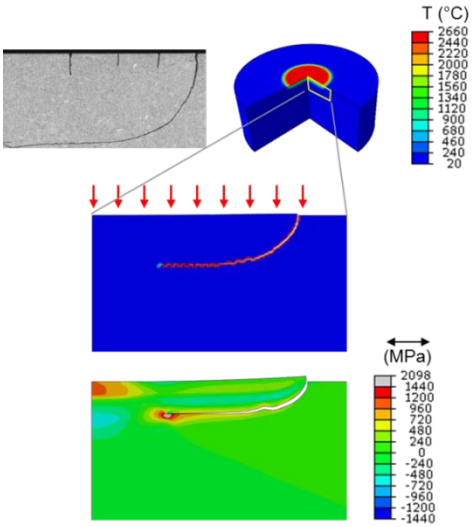

Fig. 13. Predicted crack path and stress field produced by HHF shock load of 1.27 GW/m² with pulse duration of 1 ms. A cylindrical geometry was assumed as armor model (thickness: 5 mm). The radius of the heat-loaded area is 2.26 mm [18, 19].

The XFEM study showed that the origin of the driving force of surface cracking was the strong tensile stress field (radial component) which builds up as plastically induced residual stress. This tensile residual stress is a result of the compressive radial plastic strain (1.8 %) produced locally within the heat-loaded area during the ELM-like thermal shock loading. On the contrary, the outer region surrounding the central heat-loaded area is deformed only elastically. When the HHF shock pulse is turned off, the thermal strain in the outer region is relaxed elastically trying to recover its original shape while the plastic strain in the heat-loaded area remains as permanent deformation. Thus, the elastic recovery of the surrounding region exerts a tensile traction onto the heat-loaded surface area in the radial direction during cooling. The resulting tensile stress is higher than 1000 MPa which is strong enough to cause crack initiation. This mechanism is illustrated in Fig 14 where the radial profile of the radial component of the plastic strain and radial stress are plotted for three different time points, namely, at the end of the pulse (1 ms), shortly after the pulse shut-off (2 ms) and after cooling (10 s) [18, 19].

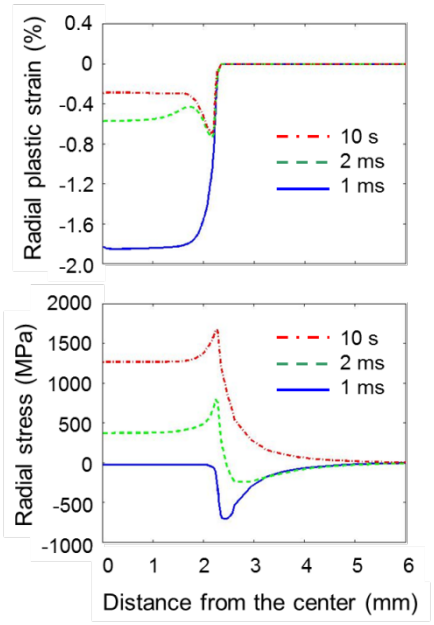

Fig. 14. Radial profile of the radial component of the plastic strain and radial stress plotted for three different time points (at the end of the HHF pulse: 1 ms, shortly after pulse shut-off: 2 ms, after complete cooling: 10 s) [18, 19].

Fig. 15 shows two distinct cracking features predicted for the same ELM-like HHF shock load (1.27 GW/m², 1 ms) [18, 19]. Fig. 15 (a) shows a crack being formed within the heat-loaded area (radial position: 1.2 mm from the center) and (b) a crack formed in the vicinity of the boundary of the heat-loaded area (at 2.24 mm). The crack formed within the heat-loaded area is short and straight whereas the crack near the boundary is long deflecting its path from the vertical to horizontal orientation parallel to the surface. This computational prediction agrees well with the experimental findings.

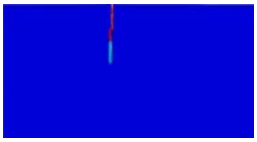
(a)
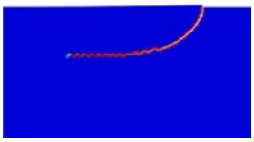
(b)

Fig. 15. Two distinct cracking features predicted for the same ELM-like HHF shock load (1.27 GW/m², 1 ms). (a): a crack being formed within the heat-loaded area (radial position: 1.2 mm from the center), (b): a crack formed near the boundary of the heat-loaded area (at 2.24 mm) [18, 19].

Summary and conclusions

The key drivers for divertor target development for a DEMO reactor are the requirements of sufficient power exhaustion capability and solid structural reliability. A successful target design should be able to assure these essential requirements for long-term operation (say, 2 full power years) and neutron irradiation accepting the transient thermal loads due to ELMs and reattachment. Given that the conventional ITER-type divertor target has been shown to fulfill the ITER specifications, the ITER concept is regarded a reasonable baseline design also for the DEMO divertor, at least for starting phase.

In order to make a design extrapolation from the ITER loading conditions to those of a DEMO, understanding of loading nature and failure features are indispensable. Some of the hitherto reported computational studies could deliver reasonable explanations on the prominent failure features observed in the previous HHF tests of ITER divertor target mock-ups. Deep cracking of W armor blocks (slow transients), surface cracking of W armor (ELMs) and plastic fatigue of soft Cu interlayer (pulsed operation) were identified as primary failure modes. Plastic fatigue of CuCrZr tube did not exhibit any fatigue risk, if there occurs no irradiation creep or overaging.

Acknowledgement

This work has been carried out within the framework of the EUROfusion Consortium and has received funding from the Euratom research and training program 2014-2018 under grant agreement No 633053. The views and opinions expressed herein do not necessarily reflect those of the European Commission.

References

[1] You J.H. et al. Fusion Eng. Des., accepted.
[2] Gilbert M.R. et al. 2012 Nucl. Fusion **52** 083019
[3] You J.H. 2015 Nucl. Fusion, 55 113026.
[4] ITER, ITER structural design criteria for in-vessel components (SDC-IC), G 74 MA 8 01-05-28 W0.2 Appendix A Materials design limit data.
[5] Timmis W. 2013 EFDA Report WP12-MAT02-M03 Copper alloys.
[6] Edwards D.J. et al. 2005 J. Nucl. Mater. 342 164-178
[7] Fabritsiev S.A. et al. 1996 J. Nucl. Mater. 233-237 127-137
[8] Fenici P. et al. 1994 J. Nucl. Mater. 212-215 399-403
[9] Li M. et al. 2009 J. Nucl. Mater. 393 36-46
[10] Rieth M. et al. 2005 J. Nucl. Mater. 342 20-25
[11] Öijerholm J. et al. J. Nucl. Mater. submitted.
[12] Li M. et al. 2015 Fusion Eng. Des. 90 88-96
[13] Pintsuk G. et al. 2013 Fusion Eng. Des. 88 1858 - 1861.
[14] Li M. et al. 2015 Fusion Eng. Des. 101 1-8.
[15] Li M. et al. 2015 Fusion Eng. Des. 89 2716-2725
[16] Hirai T. et al. 2009 J. Nucl. Mater. 390-391 751-754
[17] Pintsuk G. et al. 2013 J. Nucl. Mater. 438 S833-S836
[18] Li M. et al. 2015 J. Nucl. Mater. 457 256-265
[19] Li M. et al. 2015 Nucl. Mater. Energy 2 1-11